SUPPLEMENTARY FIGURES

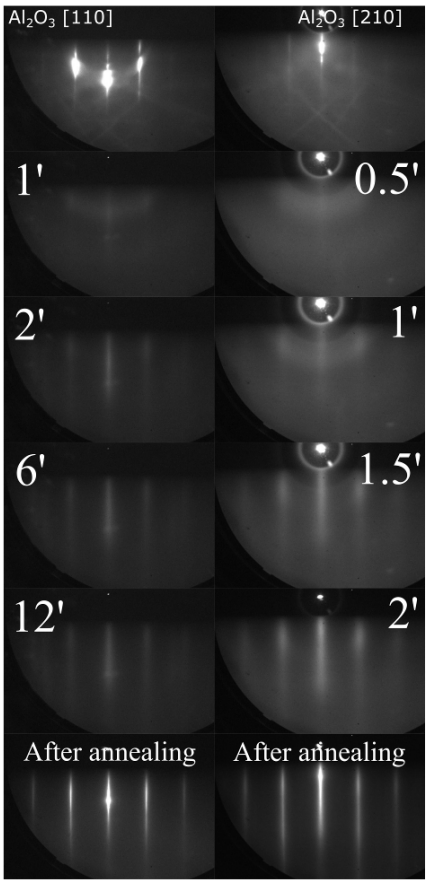

Supplementary Figure 1 **RHEED patterns during the MBE growth**. Fe_5GeTe_2 ultrathin films on Al_2O_3(001) with the e-beam aligned along the [110] and [210] direction. From top to bottom, the left panels show the evolution of the RHEED pattern during a twelve-minute growth, and the right-side panels show the same for a two-minute growth, with respective final patterns after the post-growth annealing at 550 ºC.

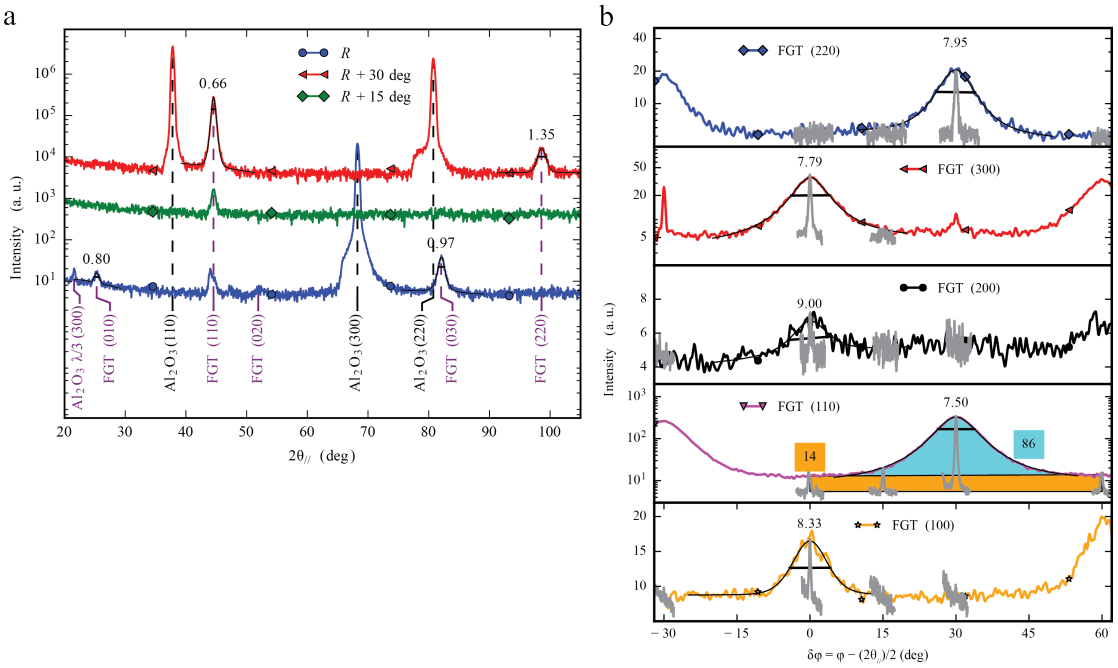

Supplementary Figure 2 **Grazing incidence X-ray diffraction of a 2 nm-thick sample. a** In-plane radial scan over the (010) reciprocal direction (R) and rotated by 15º and 30º (R+15 and R+30, respectively). Full width at half-maximum labelled on FGT Bragg peaks. **b** Azimuthal scan over the {100}, {110}, {200}, {300}, {220} families. The azimuthal distribution shows an isotropic part of 14% that is well visible on the more intense Bragg diffraction (110).

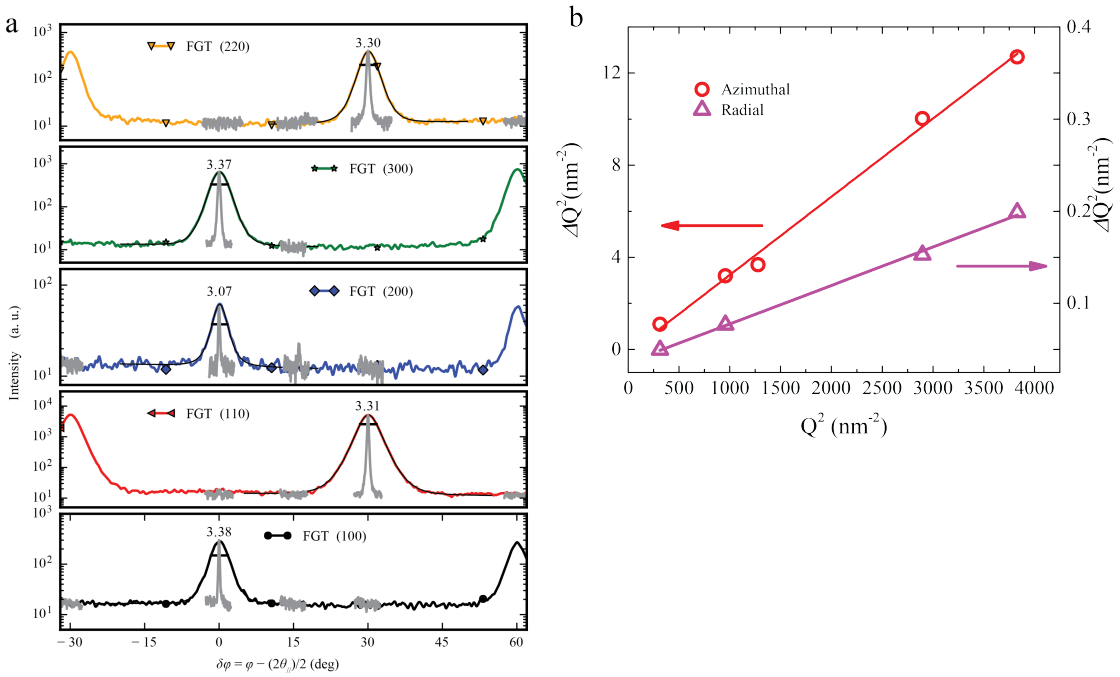

Supplementary Figure 3 **Grazing incidence XRD analysis of the 12-nm-thick film. a** In-plane azimuthal XRD scan over the families {100}, {110}, {200}, {300}, {220}, showing the 6-fold symmetry of the crystal. Grey lines show the corresponding radial peak. **b** Dispersion of the square of momentum transfer (ΔQ^2) as a function of the squared momentum transfer (Q^2) for both radial and azimuthal scans. The intercept allows for the estimation of the domain size, and the slopes for the estimation of the lattice parameter distribution (radial scan), and mosaic spread (azimuthal scan) given in the main text (see Supplementary Note 1). Solid lines are best linear fits.

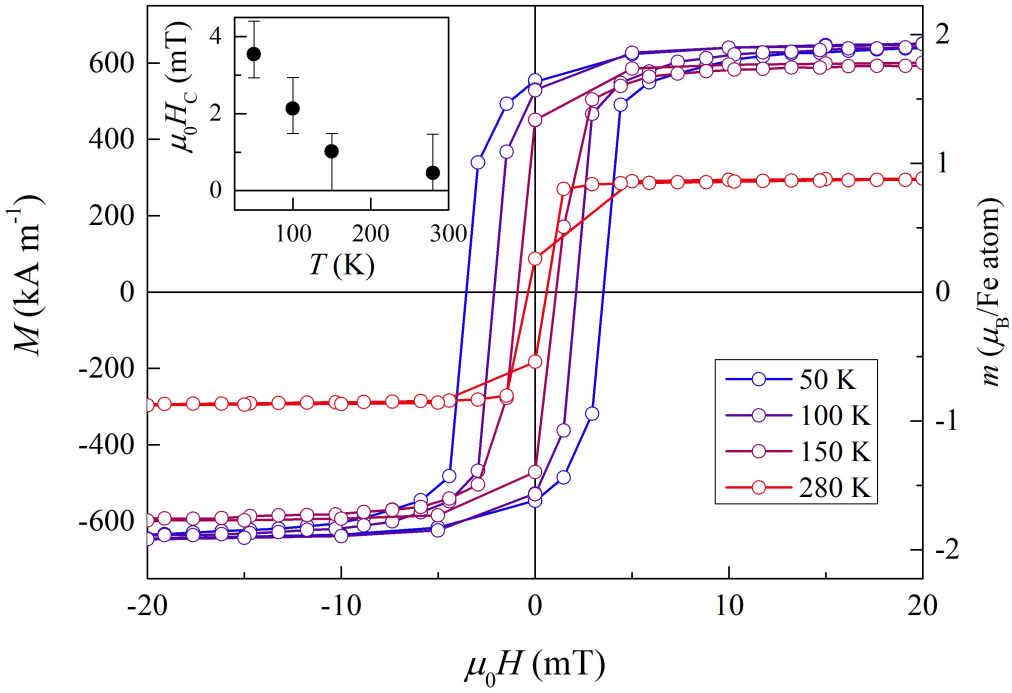

Supplementary Figure 4 **SQUID magnetization loops over low-fields.** Low field SQUID magnetization loops of the 12-nm-thick Fe_5GeTe_2 film (in-plane field). Inset: Coercive field as a function of temperature.

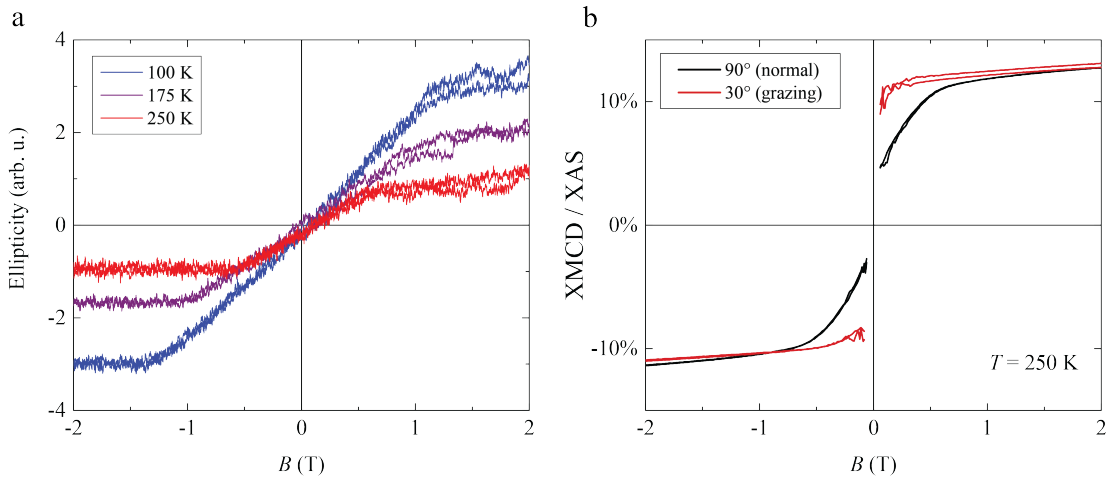

Supplementary Figure 5 **MOKE and XMDC magnetic hysteresis loops. a** Polar MOKE measurements of the 12-nm-thick film (out-of-plane field). The measurements were performed in an Oxford cryostat with optical access. A linearly polarized red laser beam (λ = 632.9 nm) illuminated the sample at normal incidence. The reflected light was analysed using a photoelastic modulator working at 42 kHz and a polarizer. The light intensity is recorded using a Si photodiode. The ellipticity is determined by a lock-in amplifier from the second harmonic measurement of the generated photovoltage. **b** XMCD field loops at 250 K at the Fe $L_{2,3}$-edge for grazing (30[a]) and out-of-plane incidence of the external magnetic field.

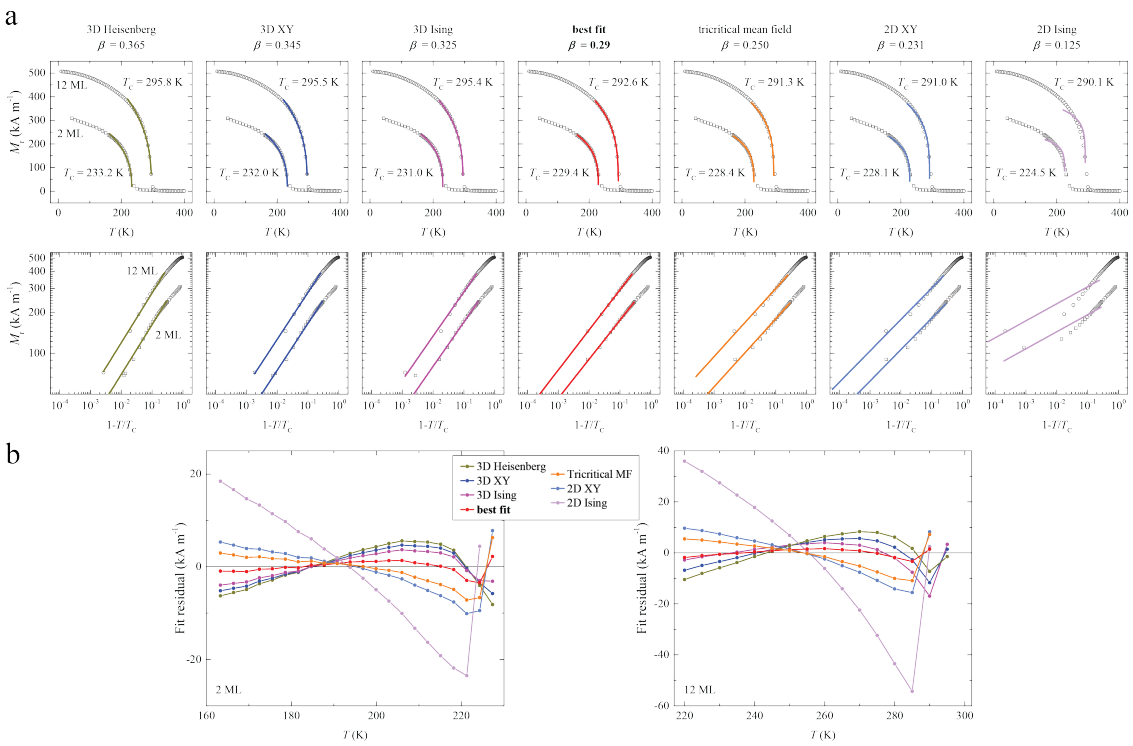

Supplementary Figure 6 **Magnetic critical exponent analysis. a** Remanent magnetization dependence on temperature for the 2 ML and 12 ML-thick films, with best fit to a scaling law $M_r = M_0 \left(\frac{T_C - T}{T_C}\right)^{\beta}$ and fitted for the magnetic critical exponents β of the 3D Heisenberg, 3D XY, 3D Ising, tricritical mean field, 2D XY, and 2D Ising models. Bottom panels show the log-log plots of the magnetization remanence as a function of 1-T/T_C. Obtained best fitting parameters for the 2 ML sample are M_0 = 337.4 ± 2.4 kA m^{-1}, T_C = 229.4 ± 0.3 K, and β = 0.29 ± 0.01. For the 12 ML sample M_0 = 572.3 ± 44.2 kA m^{-1}, T_C = 292.6 ± 2.6 K and β = 0.29 ± 0.05. **b** Residual of the fittings as a function of temperature for the various models and the best fit obtained, for the 2 ML and 12 ML-thick films.

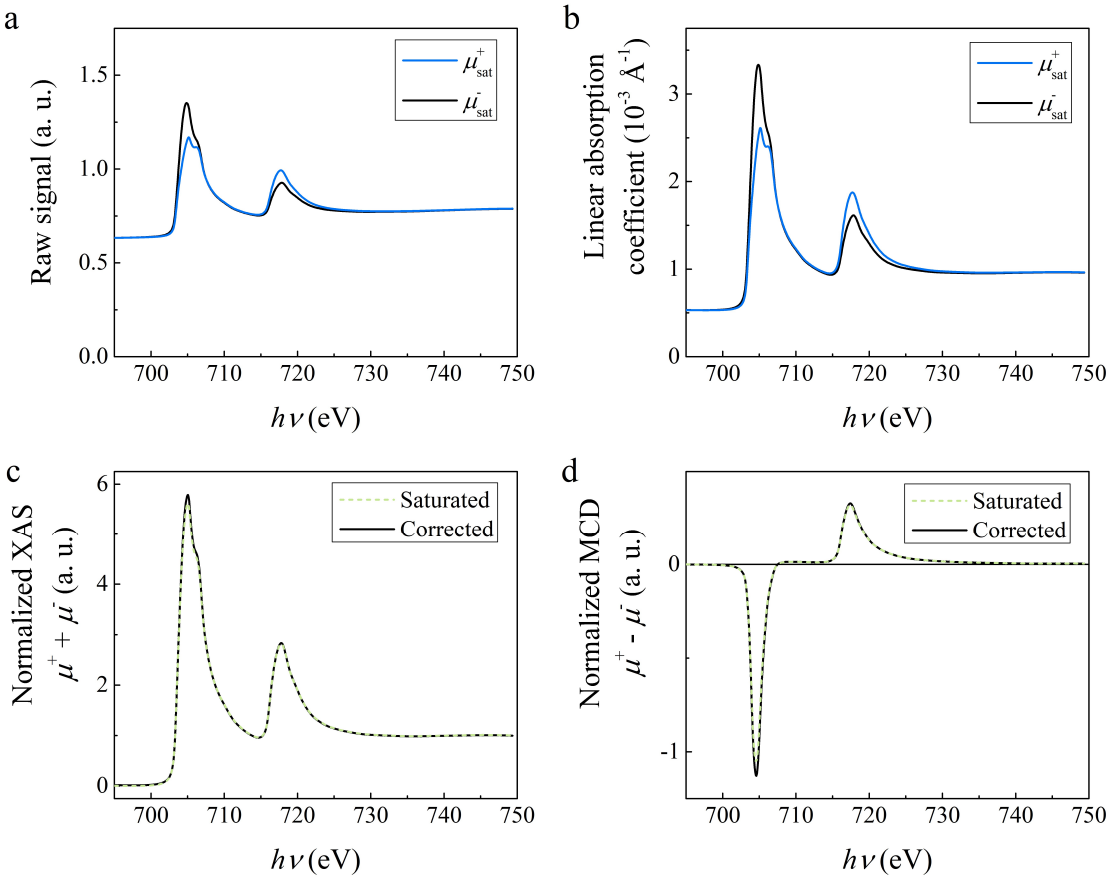

Supplementary Figure 7. **Correction of saturation effects. a** Raw absorption spectra of sample S2 (4 K, 30° incidence). **b** Linear absorption coefficient obtained by renormalization to tabulated cross sections at pre- and post-edge energies. **c** Normalized XAS ($\mu^+ + \mu^-$) spectra before and after correction of saturation effects. **d** XMCD ($\mu^+ - \mu^-$) spectra before and after correction of saturation effects.

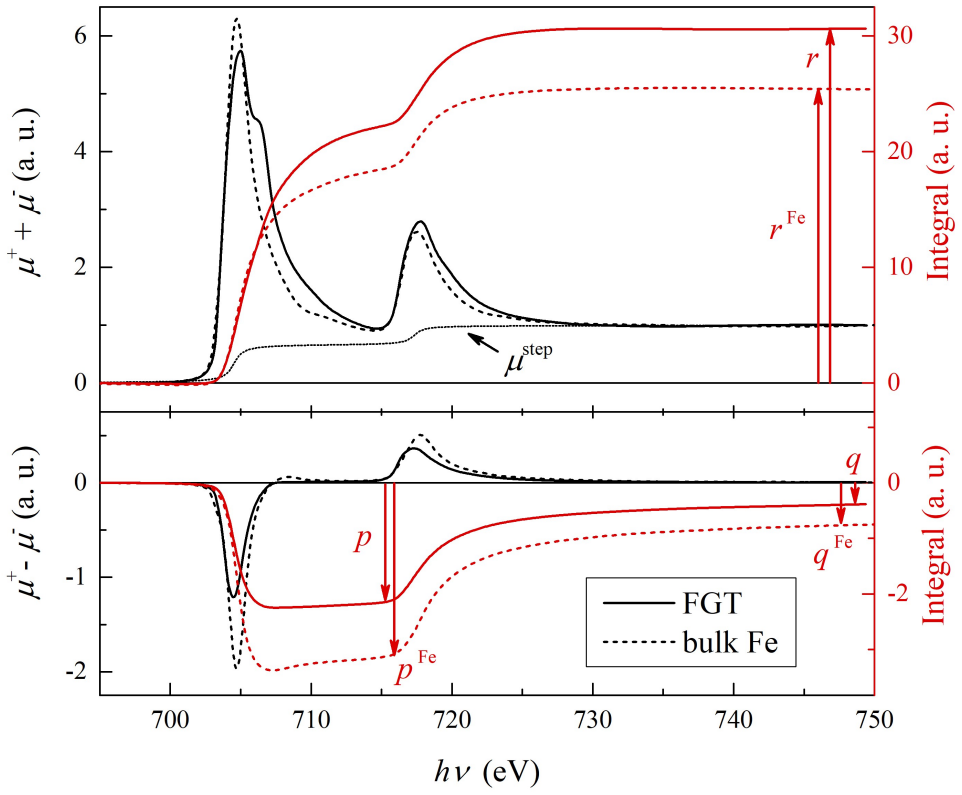

Supplementary Figure 8. **Fe $L_{2,3}$-edge analysis.** Normalized Fe $L_{2,3}$-edge XAS ($\mu^+ + \mu^-$) and XMCD ($\mu^+ - \mu^-$) spectra of Fe_5GeTe_2(12nm)/Te(5nm) (sample S2 in main text, measured at 4 K) and of a reference bulk Fe(40nm)/MgO(1nm) (measured at 300 K). In both measurements, the magnetization is saturated out-of-plane and the X-ray incidence is normal to the surface. The spectra were corrected from saturation effects. The p, q and r integrals are used to apply the sum rules. A spin moment equal to 2.1 μ_B is obtained for the bulk Fe reference sample. The relative energy shift between the two spectra is not known accurately; therefore, the L_3 peaks of both samples were artificially set at the same energy.

SUPPLEMENTARY TABLES

Supplementary Table 1 **List of parameters.** Parameters used to estimate the linear absorption of Fe_5GeTe_2 in the vicinity of the Fe *L*-edge. The atomic cross sections σ are taken from reference [1].

	d (10^{21} atom cm^{-3})	σ at pre-edge (~700 eV) (10^{-19} cm^2/atom)	σ at post-edge (~750 eV) (10^{-19} cm^2/atom)
Fe	36.4	2.0	13.8
Ge	7.3	4.6	4.6
Te	14.5	29.1	29.1

Supplementary Table 2. **Correction of saturation effects.** Magnetic moments and magnetic moment anisotropies with and without correction of saturation effects.

	m_S (μ_B/at.)	m_L (μ_B/at.)	Δm_D (μ_B/at.)	Δm_L (μ_B/at.)
Saturated	1.51	0.07	0.23	0.00
Corrected	1.54	0.08	0.21	-0.01

SUPPLEMENTARY NOTES

Supplementary Note 1: Momentum transfer versus momentum dispersion.

The momentum transfer Q for each radial Bragg diffraction peak can be calculated using $Q = \frac{4\pi}{\lambda}\sin(\theta_{//})$, and the radial and azimuthal peak momentum dispersions using $\Delta Q_{\mathrm{rad}} = \frac{\Delta(2\theta)}{2}\frac{4\pi}{\lambda}\cos(\theta_{//})$ and $\Delta Q_{\mathrm{azi}} = Q\Delta\Phi$, where $\Delta\Phi$ and $\Delta(2\theta)$ are the corresponding FWHM. Plotting ΔQ^2 as a function of Q^2 for the radial and azimuthal scans (Supplementary Figure 3b) one can determine D, $\Delta a/a$, and $\Delta\xi$ from the intercept and the slope of the radial and azimuthal scans respectively using the linearized expressions, $\Delta Q_{\mathrm{rad}}^2 = \left(\frac{2\pi}{D}\right)^2 + Q^2\left(\frac{\Delta a}{a}\right)^2$ and $\Delta Q_{\mathrm{azi}}^2 = \left(\frac{2\pi}{D}\right)^2 + Q^2\Delta\xi^2$.

Supplementary Note 2: Determination of the Fe magnetic moments with XMCD sum rules

The measured absorption spectra are first corrected from a linear background, then from saturation effects[2]. The saturated linear absorption coefficient μ_{sat} is related to the non-saturated absorption μ through:

$$\mu_{\mathrm{sat}} = \frac{1 - \exp\left[-t\left(\frac{1}{\lambda_e} + \frac{\mu}{\sin\alpha}\right)\right]}{1 + \frac{\lambda_e \mu}{\sin\alpha}}\,\mu\,, \tag{1}$$

where t is the film thickness, α the incidence angle (angle between the X-ray wave vector and the surface plane), and λ_e the electron escape depth. In order to determine μ, we adopt the following iterative procedure, which converges after a few iterations ($n \geq 2$):

$$\mu^{(0)} = \mu_{\mathrm{sat}}, \quad \xi^{(n)} = \frac{1 - \exp\left[-t\left(\frac{1}{\lambda_e} + \frac{\mu^{(n)}}{\sin\alpha}\right)\right]}{1 + \frac{\lambda_e \mu^{(n)}}{\sin\alpha}}, \quad \mu^{(n+1)} = \mu_{\mathrm{sat}}/\xi^{(n)} \tag{2}$$

The experimental total electron yield spectra (Supplementary Figure 7a) have first to be renormalized into a linear absorption coefficient by using known values at pre- and post-edge energies (Supplementary Figure 5b). We estimate the linear absorption of FGT from the tabulated cross sections of pure Fe, Ge and Te in the following way:

$$\mu_{\mathrm{sat}}(E) = \sigma_{Fe}(E)d_{Fe} + \sigma_{Ge}(E)d_{Ge} + \sigma_{Te}(E)d_{Te}, \tag{3}$$

with d_X the atomic density of element X in FGT and $\sigma_X(E)$ its atomic cross section at energy E. The values used in our analysis are reported in Supplementary Table 1. The iterative correction procedure is then applied on both μ_{sat}^{+} and μ_{sat}^{-} spectra, where + (-) refers to the parallel (antiparallel) alignment of the photon spin and magnetization (Supplementary Figure

7c,d). We assumed λ_e=1.0 nm as in pure Fe, from reference [3]. Due to the small thickness of our film (12 nm) and the dilution of Fe in the FGT alloy, saturation effects turn to be almost negligible, hardly affecting the determination of the magnetic moments (see Supplementary Table 2).

We recall below the sum rules to obtain the effective spin moment m_S^{eff} and orbital moment m_L for $L_{2,3}$ edges[4,5]. The magnetization is assumed saturated along the X-ray propagation direction.

$$m_S^{\text{eff}} = -\frac{6p - 4q}{r} N_h \tag{4}$$

$$m_L = -\frac{4q}{3r} N_h \tag{5}$$

with

$$p = \int_{L_3} (\mu^+ - \mu^-)\, \mathrm{d}E, \qquad q = \int_{L_3+L_2} (\mu^+ - \mu^-)\, \mathrm{d}E, \qquad r = \int_{L_3+L_2} (\mu^+ + \mu^- - \mu^{\text{step}})\, \mathrm{d}E,$$

N_h is the number of holes in the *d* band. μ^{step} is the absorption background due to transitions to non-*d* states and to the continuum, modeled by a double-step function with steps centered at the L_3 and L_2 edges, and having a 2:1 amplitude ratio. Supplementary Figure 8 shows μ^{step} as well as *p*, *q* and *r* integrals for the FGT sample and a bulk Fe reference. For a given incidence angle α:

$$m_S^{\text{eff},\alpha} = m_S + m_D^{\alpha} \tag{6}$$

$$m_D^{\alpha} = m_D^{\parallel} \cos^2 \alpha + m_D^{\perp} \sin^2 \alpha \tag{7}$$

$$m_L^{\alpha} = m_L^{\parallel} \cos^2 \alpha + m_L^{\perp} \sin^2 \alpha \tag{8}$$

m_S is the isotropic spin moment and m_D^{α} the intra-atomic dipole moment (asphericity of the spin density). $\parallel$ and $\perp$ refer to the in-plane and perpendicular-to-plane components, respectively. The net dipole moment amounts to zero when averaged out over the three spatial dimensions, and therefore, $2m_D^{\parallel} + m_D^{\perp} = 0$. In the main text, we report the dipole moment anisotropy $\Delta m_D = m_D^{\perp} - m_D^{\parallel} = 3m_D^{\perp}/2$, the isotropic orbital moment $m_L = \left(2m_L^{\parallel} + m_L^{\perp}\right)/3$ and the orbital moment anisotropy $\Delta m_L = m_L^{\perp} - m_L^{\parallel}$.

Combining these expressions for a set of measurements at $\alpha = 90°$ (normal incidence) and $\alpha = 30°$ (grazing incidence) yields:

$$m_S = \left(m_S^{\text{eff},90°} + 8m_S^{\text{eff},30°}\right)/9 \tag{9}$$

$$\Delta m_D = 4\left(m_S^{\text{eff},90°} - m_S^{\text{eff},30°}\right)/3 \tag{10}$$

$$m_L = \left(m_L^{90°} + 8m_L^{30°}\right)/9 \tag{11}$$

$$\Delta m_L = 4\left(m_L^{90°} - m_L^{30°}\right)/3 \tag{12}$$

To apply the sum rules on experimental spectra, one may use the theoretical number of holes for FGT, $N_h^{\text{FGT}} = 3.65$. As the white line intensity (r integral) is proportional to the number of holes, it is expected that $r^{\text{FGT}}/r^{\text{Fe}} = N_h^{\text{FGT}}/N_h^{\text{Fe}}$. However, by comparing our measurements

to a reference bulk Fe sample, we find $r/r^{\mathrm{Fe}} = 1.21 \neq N_h^{\mathrm{FGT}}/N_h^{\mathrm{Fe}} = 1.08$ (with $N_h^{\mathrm{Fe}} = 3.39$). This suggests that the absorption signal of our FGT sample might contain an additional contribution, possibly due to some surface oxidation despite the Te capping layer ($r = r^{\mathrm{FGT}} + r^{\mathrm{FeO_x}}$). Indeed, the high-energy shoulder on the L_3 absorption peak turns to be more intense than reported in reference[6], which could be consistent with partial oxidation of the top-most FGT layer. This does not prevent us to estimate the FGT magnetic moments. We note that there is no MCD observed at the energy of the peak shoulder (the oxidized Fe is nonmagnetic). Therefore, $p = p^{\mathrm{FGT}} + p^{\mathrm{FeO_x}} \approx p^{\mathrm{FGT}}$ and $q = q^{\mathrm{FGT}} + q^{\mathrm{FeO_x}} \approx q^{\mathrm{FGT}}$. The FGT spin moment m_S^{FGT} and orbital moment m_L^{FGT} write:

$$m_S^{\mathrm{FGT}} = -\frac{6p^{\mathrm{FGT}} - 4q^{\mathrm{FGT}}}{r^{FGT}} N_h^{FGT} \approx -\frac{6p - 4q}{r} \times \frac{r}{r^{FGT}} N_h^{\mathrm{FGT}} = -\frac{6p - 4q}{r} \times \frac{r}{r^{\mathrm{Fe}}} N_h^{\mathrm{Fe}} \quad (13)$$

$$m_L^{\mathrm{FGT}} = -\frac{4q^{\mathrm{FGT}}}{3r^{\mathrm{FGT}}} N_h^{\mathrm{FGT}} \approx -\frac{4q}{3r} \times \frac{r}{r^{\mathrm{FGT}}} N_h^{\mathrm{FGT}} = -\frac{4q}{3r} \times \frac{r}{r^{\mathrm{Fe}}} N_h^{\mathrm{Fe}} \quad (14)$$

We then used the experimentally determined r/r^{Fe} and the number of holes of bulk Fe $N_h^{\mathrm{Fe}} = 3.39$. The magnetic moments directly estimated with $N_h^{\mathrm{FGT}} = 3.65$ are 12% larger than the values given in the main text and are indicated as an upper error bar in Fig. 4f in the main text.

Note that the total electron yield detection is extremely sensitive to the surface. In contrast, SQUID measurements probe the full layer. We thus assume that the surface oxidation contributes marginally to the SQUID signal.

SUPPLEMENTARY REFERENCES

1. Saloman, E. B., Hubbell, J. H. & Scofield, J. H. X-ray attenuation cross sections for energies 100 eV to 100 keV and elements Z = 1 to Z = 92. *At. Data Nucl. Data Tables* **38**, 1–196 (1988).
2. Nakajima, R., Stöhr, J. & Idzerda, Y. U. Electron-yield saturation effects in L-edge x-ray magnetic circular dichroism spectra of Fe, Co, and Ni. *Phys. Rev. B* **59**, 6421–6429 (1999).
3. Jablonski, A. & Powell, C. J. NIST Standard Reference Database 82. *NIST* https://www.nist.gov/srd/nist-standard-reference-database-82 (2010).
4. Chen, C. T. *et al.* Experimental Confirmation of the X-Ray Magnetic Circular Dichroism Sum Rules for Iron and Cobalt. *Phys. Rev. Lett.* **75**, 152–155 (1995).
5. Stöhr, J. Exploring the microscopic origin of magnetic anisotropies with X-ray magnetic circular dichroism (XMCD) spectroscopy. *J. Magn. Magn. Mater.* **200**, 470–497 (1999).
6. Yamagami, K. *et al.* Itinerant ferromagnetism mediated by giant spin polarization of the metallic ligand band in the van der Waals magnet Fe5GeTe2. *Phys. Rev. B* **103**, L060403 (2021).